NDT&E International 141 (2024) 102990

Contents lists available at ScienceDirect

NDT and E International

journal homepage: www.elsevier.com/locate/ndteint

Research Paper

Automatic estimation of surface and probe location for 3D imaging with bidimensional arrays

Guillermo Cosarinsky [a,b,c,*], Jorge F. Cruza [a], Mario Muñoz [a,c], Jorge Camacho [a]

[a] Ultrasound Systems and Technology Group (GSTU), Institute for Physical and Information Technologies (ITEFI), Spanish National Research Council (CSIC), c/Serrano 144, 28006 Madrid, Spain
[b] Non Destructive Testing Department, National Atomic Energy Commission (CNEA), Av. Gral. Paz 1499, Buenos Aires B1650, Argentina
[c] Electronics Department, Escuela Politécnica, Universidad de Alcalá de Henares, Ctra.Madrid-Barcelona, Km. 33, 600, 28805 Madrid, Spain

ARTICLE INFO

Keywords:
Ultrasound imaging
3D imaging
2D array
Matrix array
Surface detection
Refraction

ABSTRACT

Ultrasound imaging for Non Destructive Testing is frequently performed in an immersion setup, where water is used as coupling medium between the probe and the component under test. For the computation of the time delays needed for beam-forming, the shape of the component surface and probe location and orientation (PLO) must be known. In this work we develop methods for the automatic detection of the surface and the estimation of PLO for 2D array probes. In particular, the methods developed apply to three types of elementary surfaces which are usually found in industrial and structural components: planes, cylinders and spheres. The methods use the measured surface echoes Time of Flight (TOF) to fit parametric models based on ray propagation and reflection on the surface, giving the coordinates and Euler angles that define the PLO relative to the component under test. Validation experiments with four test specimens representing the three types of surfaces are presented . The accuracy and precision of estimated PLO coordinates and angles are analyzed, and a Total Focusing Method (TFM) imaging example is shown achieving a correct detection of artificial defects in the component for a different PLOs.

1. Introduction

Ultrasound transducer arrays have become a fundamental tool in Non Destructive Testing (NDT) [1,2] with a broad range of applications from welding inspection to composite structures. The most frequently used type of probes are linear arrays, composed of elongated elements in a linear arrangement, which enable beam focusing and steering inside a plane. This limitation can be overcome using 2D arrays [3]. In this type of probes the transducer elements are distributed on a 2D region, enabling beam steering and focusing in all spatial directions [4,5]. The present work is about the use of 2D arrays in immersion testing configurations.

Immersion testing is widely used in NDT as coupling technique when rigid wedges are difficult or impossible to use, as in the case of components with curvature changes or when contact coupling cannot be guaranteed throughout the inspection because of mechanical constrains. In order to compute the ray paths needed for imaging algorithms, the probe location and orientation (PLO) relative to the component under test must be known. Additionally, the surface shape must be also known. This information defines the geometry needed for the two-point ray tracing [6] between each array element and each image point. In this work we address the problem of estimating the PLO of the probe using the surface reflection echoes for some primitive shapes: plane, cylindrical and spherical surfaces. These shapes are representative of some common inspection cases like tubes, rods and laminates, and can be used to locally describe the shape of more complex geometries, like carbon fiber stringers in aerospace industry or pipe elbows in energy or petrochemical fields.

The problem of ultrasound surface estimation for imaging through a coupling medium (usually water in the immersion testing case) was tackled by many authors for the case of linear arrays. The developed methods use different types of acquisitions and different signal processing algorithms, which can be divided in two main classes. In one case the time of flight (TOF) of the surface echoes is first extracted from the signals and the surface points are computed with those TOFs. This approach is used in Refs. [7–10] with pulse–echo and pitch–catch acquisitions. In [11] this approach is also followed, further proposing a method using plane wave acquisition.

* Corresponding author at: Ultrasound Systems and Technology Group (GSTU), Institute for Physical and Information Technologies (ITEFI), Spanish National Research Council (CSIC), c/Serrano 144, 28006 Madrid, Spain.
E-mail address: g.cosarinsky@csic.es (G. Cosarinsky).

https://doi.org/10.1016/j.ndteint.2023.102990
Received 2 September 2023; Received in revised form 31 October 2023; Accepted 4 November 2023
Available online 18 November 2023

The second class of algorithms is imaging based: by using Full Matrix Capture (FMC) and the Total Focusing Method (TFM) [12], an image of the first propagation medium is formed by using rectilinear ray paths. In this image the component surface appears as a narrow region of high intensity, which is used to reconstruct the surface geometry. In [8] the authors compare a TFM-based method with TOF-based methods, concluding that TFM method is more accurate but slower. In fact, it requires the processing of all signals instead of just a set of TOFs. In [9] a different imaging based algorithm is proposed, which does not need the formation of entire images. It also proposes a TOF-based method and compare both to the pitch–catch method proposed in [11], concluding that the three methods were almost equivalent in accuracy, being pitch–catch the fastest one.

A TFM-based surface extraction method is also presented in [13] along with a form of Synthetic Aperture Focusing Technique (SAFT) alternative. This work applies these methods to the scanning of bony surfaces for robotic knee arthroplasty, achieving average errors of about 0.8 mm. Another work using TFM for surface extraction is [14], in which the authors analyze in depth how estimation errors increase in zones where the surface normal forms a high angles with the probe face normal. They report less than 1 mm errors in the "low" slope zones, but larger than 1 mm in steeper zones.

The methods developed in the aforementioned works only apply to 2D geometries. They are used to estimate a curve which is the surface cross section. For them to work properly, the surface normal must be contained in the array imaging plane. If not, waves reflected on the surface would be directed out of plane, resulting in insufficient acoustic energy being received and incorrect focusing delays.

In practical situations, the problem of ensuring the perpendicularity of the array plane with the component surface during the whole scan, makes mechanical design much more complex. Moreover, it usually limits the inspection speed and restricts the kind of parts that can be evaluated with a given automated machine. Finally, if the component under test presents a doubly curved and non-developable surface, the inspection with a linear array cannot warranty the best possible image.

A solution to this problem is using 2D arrays, which can detect the surface and apply correct focal laws in any spatial direction. Nevertheless, few works have been presented so far about the problem of automatic surface and probe location detection and focusing with these devices in NDT. In [15] a TFM-based surface extraction method is proposed for 2D arrays, and a TOF-based pulse–echo method was proposed by our group in [16].

All the approaches reported above estimate a set of surfaces points representing a local patch, and they can be applied to arbitrary shaped surfaces. In this work we propose a method for parametric estimation, which can be considered as an inverse problem [17]. A solution is given for some elementary shapes often found in mechanical and structural components, and for which the forward problem (computation of surface echoes TOF) can be solved with closed formulae. The corresponding models are derived in Section 2. In Section 3 validation experiments are presented and the results are discussed in Section 4.

2. Methods

The setup we are going to analyze is composed of a probe immersed in a homogeneous propagation medium (medium 1) with propagation speed c_1, and a test component in the same medium with a boundary surface S.

The probe is an array of N transducer elements distributed on a plane region F (the probe active face or aperture) (Fig. 1.a). The elements in a 2-dimensional (2D) array like this might also be distributed on a curved surface [18], but in this work only the flat case will be considered. As shown in Fig. 1 a Probe Coordinate System (PCS) with Cartesian axes (u, v, w) is attached to the probe face, such the array face is on the plane (u, v). The origin of coordinates is a point O_P on the array face, which we will call the probe face center.

The probe transmits a wave that reflects on the surface S and the array elements receive the echoes recorded on A-scans $A(i, t)$ where i is the element index and t is time. For each A-scan there will be a strong echo from the surface (which we are going to suppose originated at a specular reflection point) arriving at a time $t_S(i)$. The hypothesis of specular reflection restricts the analysis to smooth surfaces compared to the wavelength. The arrival times might be estimated from the signals by different methods [19,20], being threshold crossing the simplest one, which we are going to use for our experiments in Section 3.

Two types of emitted waves will be considered: single element emission and plane wave emission. In the single element emission, the wave is idealized as a spherical wave radiated from a point source in the element center. This is a good approximation as long as the element size has similar dimensions as the wavelength, and the reflecting surface is in the far field. With this two types of emitted waves, time of flight (TOF) is easily computed to any field point.

The objective of this section is to derive equations to estimate probe location an orientation (PLO) relative to S, given the element distribution and the set of arrival times of the surface echoes. The element distribution is defined by the position of elements center points $E(i)$, which can be described by the coordinates $(u(i), v(i))$ in the PCS of the vectors $\overline{O_P E}$. In the case of the so-called matrix arrays 2, like those used in this work's experiments, the elements are arranged in a rectangular grid, and so the natural way to index them is using two indexes (i, j). The element coordinates in the PCS are, therefore:

$$\begin{cases} u(i) = \left(i - \dfrac{N_u - 1}{2}\right) p_u \\ v(j) = \left(j - \dfrac{N_v - 1}{2}\right) p_v \end{cases} \tag{1}$$

Where (N_u, N_v), (p_u, p_v) are the number of elements and pitches in each direction Fig. 2.b. The coordinate origin O_P is chosen in the geometrical center of the probe face, and the index intervals are $i \in [0, N_u - 1]$ and $j \in [0, N_v - 1]$.

The shape of S and the PLO relative to S are defined in a World Coordinate System (WCS) with Cartesian axes (x, y, z) and origin in a point O_W (Fig. 1.a). PLO can be defined by the position vector $\overline{O_W O_P}$ of probe face center (point O_P), and a rotation matrix M_{rot} relating PCS and WCS. This rotation can be parametrized using three angles $\Theta = (\theta_x, \theta_y, \theta_z)$, the so-called Euler angles [21]. Thus, 6 numbers are needed to define probe location and orientation. The position vector of an array element E (using for simplicity the same symbol to denote the element and its center point) can thus be expressed in the WCS as:

$$\left|\overline{O_W E}\right|_W = \begin{pmatrix} E_x \\ E_y \\ E_z \end{pmatrix} = \left|\overline{O_W O_P}\right|_W + M_{rot} \begin{pmatrix} u \\ v \\ 0 \end{pmatrix} \tag{2}$$

where we use the notation $|\ |_W$ for coordinates in WCS, and we denote by (E_x, E_y, E_z) the coordinates of E. Let us suppose we know a function g (the model) such that:

$$t_S(i) = g(i, O_P, \Theta, \Omega) \tag{3}$$

where Ω are a set of parameters that define the surface geometry in WCS and $t_S(i)$ the theoretical two-way time-of-flight from element i to the surface point with specular reflection. . Then if the measured times of arrival are $t^*_S(i)$, least squares fitting [17] of the model parameters can be done by minimization of the cost function:

$$Cost(i, O_P, \Theta, \Omega) = \sum_{i=0}^{N-1} \left(w(i)\left(t^*_S(i) - t_S(i)\right)\right)^2 \tag{4}$$

where $w(i)$ are weights that could be chosen as 1 for every element or computed by some criteria related with the quality or uncertainty of the measurement (more on this in Section 3). The fitted parameters define the surface shape and the probe position. In the case that the

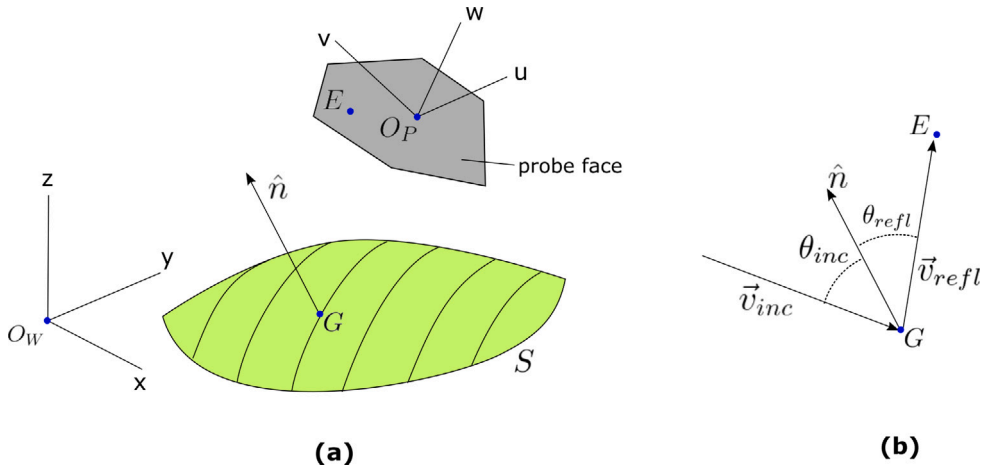

Fig. 1. Setup schematic. (a) Coordinate systems, array face, and test component surface. (b) Vectors involved in the reflection law.

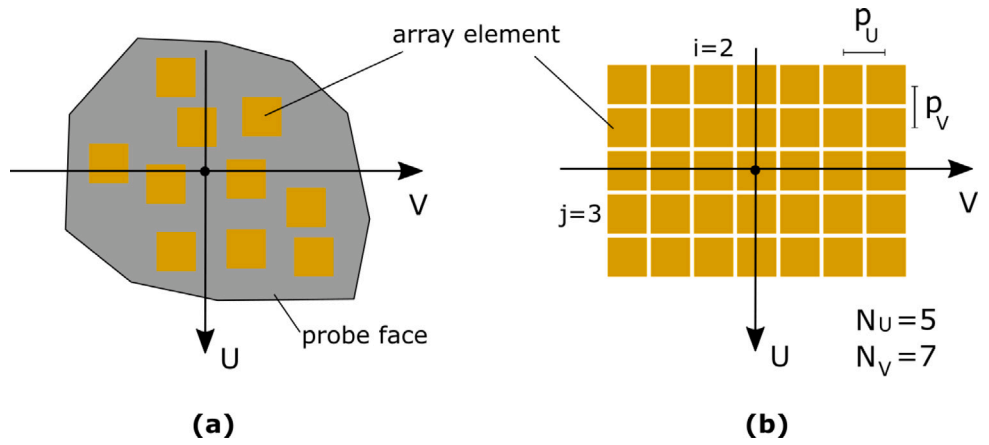

Fig. 2. 2D transducer array. Probe face element distribution. (a) Arbitrary distribution, (b) Matrix array.

surface shape is already known, this procedure can be used to estimate the PLO parameters.

The modeling function g depends on the type of transmitted wave and the type of geometry. To compute the arrival time for a receiving element E, the point G on S where the incident wave is reflected towards E must be determined. This point G should satisfy the law of reflection (Fig. 1.b): the incident ray $\vec{v}_{inc}$, the reflected ray $\vec{v}_{refl}$ and the surface normal $\hat{n}$ at G must lie in the sample plane (the so-called incidence plane) and the incidence angle θ_{inc} (included angle between $\vec{v}_{inc}$ and $\hat{n}$) and reflection angle θ_{refl} (included angle between $\vec{v}_{refl}$ and $\hat{n}$) must be equal. Once G is known, the arrival time is computed as:

$$t_S = t_{inc} + \frac{1}{c_1}\left\|\overline{GE}\right\| \tag{5}$$

Where t_{inc} is the time take by the emitted (incident) wave to arrive to G. Both t_{inc} and $\vec{v}_{inc}$ depend on the transmitted wave. The distance $\left\|\overline{GE}\right\|$ is computed in WCS using (2) for the element coordinates. In the case of single element transmission, for a transmitting element E_{tx}:

$$\begin{aligned} \vec{v}_{inc} &= \left\|\overline{GE_{tx}}\right\| \\ t_{inc} &= \frac{1}{c_1}\left\|\vec{v}_{inc}\right\| \end{aligned} \tag{6}$$

In the case of plane wave emission, let $\vec{v}_{pw}$ be the unitary direction vector of the wave (normal to the wavefronts), then:

$$\begin{aligned} \vec{v}_{inc} &= \vec{v}_{pw} \\ t_{inc} &= \frac{1}{c_1}\vec{v}_{pw}\cdot\overline{O_P G} \end{aligned} \tag{7}$$

where the $\cdot$ is the dot product between two vectors. The distances $\left\|\overline{GE}\right\|$ and $\left\|\vec{v}_{inc}\right\|$ are computed in WCS using (2) for the element coordinates.

For an arbitrary surface shape, given a transmitted wave, finding G for each receiving element is a problem with no closed solution: it must be solved by an iterative algorithm. It is a root finding problem of two variable function. However, for some simple geometries a closed formula can be found. In the following sections we will analyze some particular cases were an analytical expression for function g can be derived, at least approximately. The surface types we are going to analyze are plane, cylindrical and spherical surfaces, which are representative of usual NDT inspection problems, and can be also used to locally describe more complex geometries.

2.1. Pulse–echo acquisition

For this method, each array element E transmits and receives (thus the pulse–echo name) sequentially. Thus N transmission are used, and a single element receiving aperture. In this case, as the emitter and receiver are the same element, $\theta_{inc} = \theta_{refl} = 0$, and the vector $\overline{GE}$ is parallel to $\hat{n}$ (Fig. 1.b).

2.1.1. Plane surface

The simplest possible geometry is a plane surface (Fig. 3.a). The WCS can always be chosen such that S is the XY-plane (z=0), and $\hat{n} = \hat{z}$ where $\hat{z}$ is the unitary vector in z-direction. Besides, O_W is selected such that the probe center is on the z-axis, $\left|\overline{O_W E}\right|_W = (0, 0, O_{P,z})$ In this case G is such that:

$$\left\|\overline{GE}\right\| = \overline{O_W E}\cdot\hat{z} \tag{8}$$

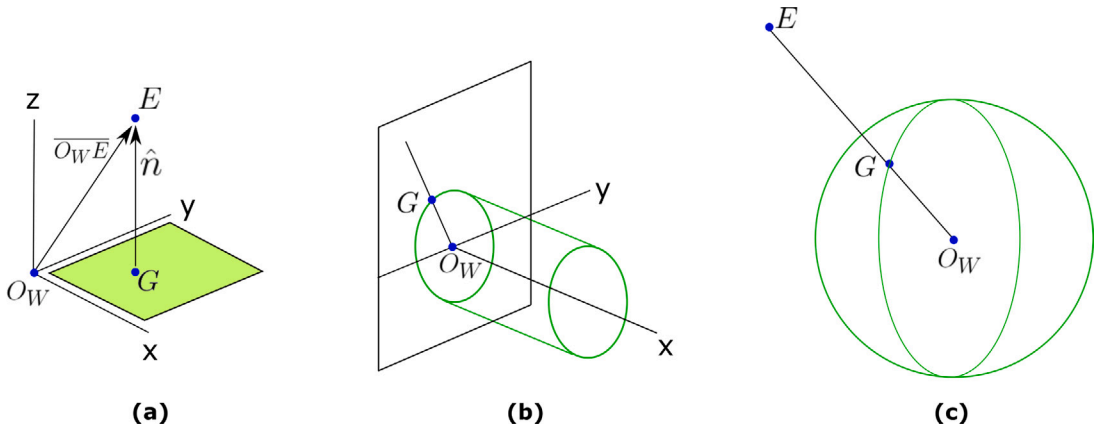

Fig. 3. Simple geometries where the incidence point G can be easily found. (a) Plane surface, (b) Cylindrical surface, (c) Spherical surface.

where we suppose the probe above S (this convention is used throughout this article). In other words, $\left\|\overline{GE}\right\|$ is the z coordinate of element E, which is computed with Eq. (2). Eq. (5) thus becomes:

$$t_S = \frac{2}{c_1} E_z \tag{9}$$

The rotation matrix can be parametrized with only 2 angles, because a rotation around de z-axis does not affect the arrival times. The total number of parameters to be fitted is then only 3.

2.1.2. Cylindrical and spherical surfaces

Another simple geometry is a cylindrical surface. In this case WCS can be chosen such that the cylinder axis is the x-axis. Thus, the only parameter needed to define the cylinder is its radius R_{cyl}. If we draw a line from E to the cylinder axis and orthogonal to the latter, then G is the intersection between the said line and the cylinder (Fig. 3.b). The normal $\hat{n}$ at G is parallel to $(0, E_y, E_z)$, and hence:

$$t_S = \frac{2}{c_1}\left(\sqrt{E_y^2 + E_z^2} - R_{cyl}\right) \tag{10}$$

Taking advantage of the translational symmetry, WCS is chosen such that $\left|\overline{O_W E}\right|_W = (0, O_{P,y}, O_{P,z})$ and the rotational symmetry of the cylinder allows to set the Euler angle corresponding to rotation around x-axis to be fixed as zero.

For a radius R_{sph} spherical surface (Fig. 3.c) the geometry is very similar. If O_W is chosen in the sphere's center, then:

$$t_S = \frac{2}{c_1}\left(\sqrt{E_x^2 + E_y^2 + E_z^2} - R_{sph}\right) \tag{11}$$

In this case any configuration can be described by $\left|\overline{O_W E}\right|_W = (O_{P,x}, O_{P,y}, O_{P,z})$ and no Euler angle is needed, because the spherical symmetry allows WCS to be chosen in such a way that the probe face is aligned to the axes.

In the cylindrical case 5 parameters $(y, z, \theta_y, \theta_z, R_{cyl})$ are needed to define the geometry, and 4 parameters (x, y, z, R_{sph}) are needed in the spherical case.

It is worth to mention that the planar, spherical and cylindrical cases are particularly interesting for local estimation of the surface, because more complex geometries can be constructed by the junction of these simpler cases.

2.1.3. Reflection on the concave side of a cylinder or sphere

In the previous sections the probe was facing the convex side of either cylinder or sphere. But, what happens if the probe emits towards the concave side? The geometrical reasoning is equivalent, but now there are two diametrically opposite points G and G' that satisfy the reflection law (Fig. 4). As the array element E only radiates to a half-space (indicated by the main lobe arrow in Fig. 4), only one of those points is physically realized. In one case (Fig. 4.a) the physical ray is shorter that the radius, and in the other case (Fig. 4.b) the physical ray is larger than the radius. Hence, for the pulse–echo method, Eqs. (10) and (11) must be modified as follows:

$$t_S = \frac{2}{c_1}\left(R_{cyl} \pm \sqrt{E_y^2 + E_z^2}\right) \tag{12}$$

$$t_S = \frac{2}{c_1}\left(R_{cyl} \pm \sqrt{E_x^2 + E_y^2 + E_z^2}\right) \tag{13}$$

The sign of the sum in equations is chosen by following the explained criterion: - for the case in Fig. 4.a, and + for the case in Fig. 4.b.

2.2. Pitch–catch acquisition

In this case, for each transmission event, a single element E_{tx} is excited and an another element E receives the echo. This element belongs to a chosen reception aperture, that might be the whole array if enough parallel channels are available.

A simple analytical method to find the point G in this case is only available for the plane surface. For a spherical surface, finding G is a famous mathematical problem: the Alhazen's problem, in honour to the Arabian medieval mathematician and astronomer Ibn al Haytham (latinized as Alhazen), who provided the first published solution to the problem by using an intricate geometrical construction [22]. Analytical solutions for the sphere and for quadric surfaces in general are provided in [23] in terms of roots of polynomials in the complex plane. Those roots must be computed by numerical methods. Thus, for each pair of array elements a numerical roots finding algorithm must be executed resulting in a heavy computational load.

We propose in this work two approximate methods that provide closed formulas to solve the problem. In the first approximation, a small receiving subaperture around E_{tx} is used, such that a receiving element E is close to E_{tx} (compared to curvature radius) and the local tangent plane (Fig. 5.b) can be used to approximate the surface. The problem is thus reduced locally to the plane surface, which has a closed solution as will be exposed below. On the other hand, if the complete array aperture is used in reception, we propose an approximation method based on the spherical (or circular) mirror equations from geometrical optics [24].

2.2.1. Plane surface

The law of reflection states that the angles θ_{inc} and θ_{refl} (Fig. 5.a) by the incident and reflected rays with the surface normal at the reflection point are always equal. This implies that, as illustrated in Fig. 5.a, the ray path from E_{tx} to E has the same length as the straight line that joins E with E_{tx}^*, the specular image of E_{tx} created by the reflecting plane (Fig. 5.a). The time of flight is thus given by:

$$t_S = \frac{1}{c_1}\left\|\overline{E_{tx}^* E}\right\| \tag{14}$$

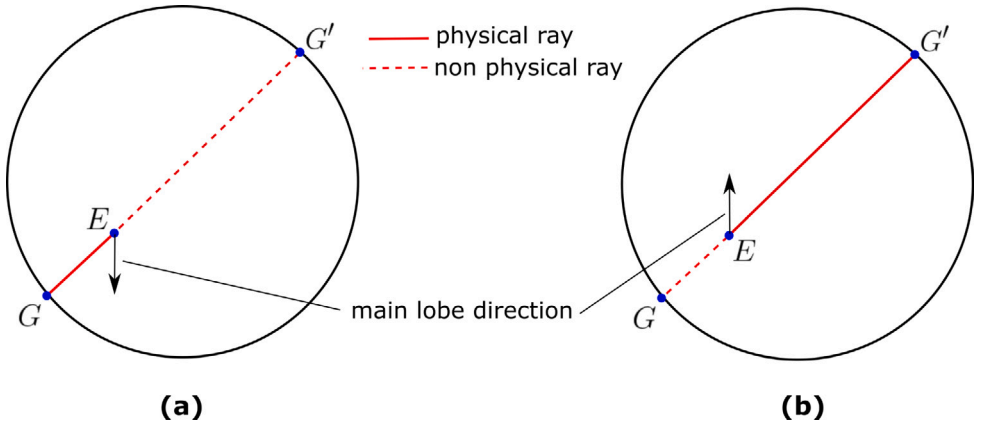

Fig. 4. Cross section of cylinder or sphere containing an array element. Schematic of the criterion to choose the correct reflection point. (a) and (b) show the two possible cases for the reflection point in the pulse–echo mode.

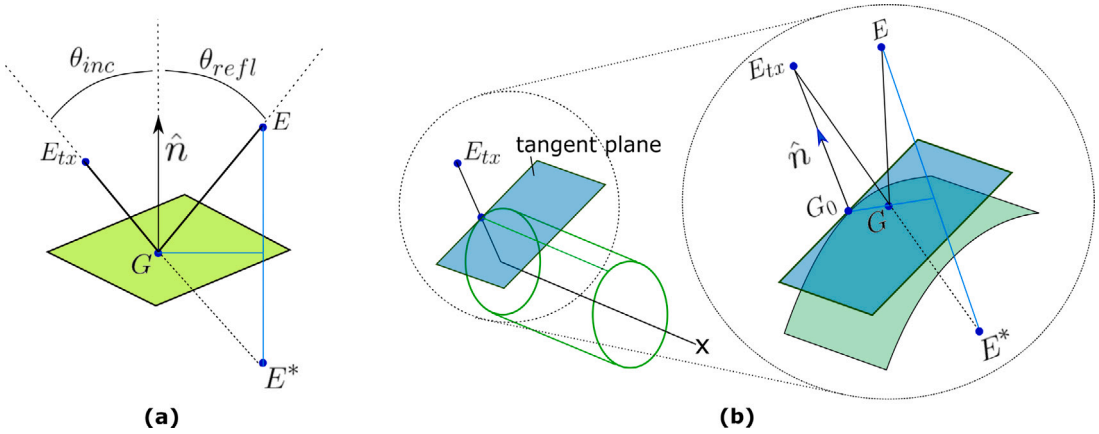

Fig. 5. Geometry for the pitch-catch method. (a) Law of reflection and mirror image (b) Reflection at the tangent plane.

Using as before a WCS such that the reflecting plane is the XY plane, the coordinates of E^*_{tx} are $(E_{tx,x}, E_{tx,y}, -E_{tx,z})$, and Eq. (12) becomes:

$$t_S = \frac{1}{c_1}\sqrt{(E_x - E_{tx,x})^2 + (E_y - E_{tx,y})^2 + (E_z + E_{tx,z})^2} \tag{15}$$

2.2.2. Cylindrical and spherical surfaces

Let us call G_0 to the point G in the pulse–echo case (G point in Fig. 3.b). If we use a small reception aperture such that receiver E is close enough to the transmitter E_{tx} ($\left\|\overline{E_{tx}E}\right\| \ll R_{cyl}$), then G is close to G_0. Therefore, we can approximate the cylindrical surface in the vicinity of G_0 by the tangent plane (Fig. 5.b), and use the method explained before for a plane surface. To find the specular image of E_{tx} through the tangent plane we use the projection of the vector $\overline{G_0E_{tx}}$ onto the plane normal $\hat{n}$. From Fig. 5.b:

$$\overline{O_W E^*_{tx}} = \overline{O_W E_{tx}} - 2(\overline{G_0 E_{tx}} \cdot \hat{n})\hat{n} \tag{16}$$

where $\hat{n}$ and G_0 are give by:

$$|\hat{n}|_W = \pm\frac{(0, E_y, E_z)}{\sqrt{E_y^2 + E_z^2}} \tag{17}$$

$$\overline{O_W G_0} = \pm R_{cyl}\hat{n} \tag{18}$$

and the sign $\pm$ is selected according to the criteria explained in Section 2.1.3 Using Eqs. (16), (17) and (18), the specular image of the emitter is found and TOF is computed by Eq. (14)

An analogous procedure is used for the spherical surface, the only difference being how $\hat{n}$ and G_0 are computed:

$$|\hat{n}|_W = \pm\frac{(E_x, E_y, E_z)}{\sqrt{E_y^2 + E_z^2}} \tag{19}$$

$$\overline{O_W G_0} = \pm R_{sph}\hat{n} \tag{20}$$

This pitch–catch method works as an extension of the pulse–echo method presented in Section 2.1. Both of them might be subject of a problem schematized in Fig. 6: the angle α formed by the ray with normal incidence could be too large for the angular sensitivity of the array element, resulting in very low amplitude surface echoes. This issue impacts the concave case (6.b) more than the convex one (6.a).

To solve this problem, we propose an alternative in which the whole array aperture is used in reception, in such a way that is more probable to catch more energetic rays. When using the whole aperture, the distance of a receiving element to the emitter might be too large for the G_0 tangent plane approximation. We can apply in this case the geometrical optics model [24] of the spherical mirror, illustrated in Fig. 7. The mirrors optical axis (Fig. 7.b) is the line passing through the vertex V and the circle center. In the paraxial approximation, all the rays coming from an object (point **Ob** in Fig. 7) which are reflected by the mirror pass through a real or virtual image (point **Im** in Fig. 7). To define the positions of the object and its image a coordinate system VCS with origin at V is used. The first VCS axis is coincident with the first WCS, and the third axis is the optical axis (Fig. 7). A radius R mirror has a focal point with VCS coordinates $(0, 0, f)$ where $f = \pm\frac{R}{2}$, + for the concave case (Fig. 7.a) and - for the convex one (Fig. 7.b). The VCS

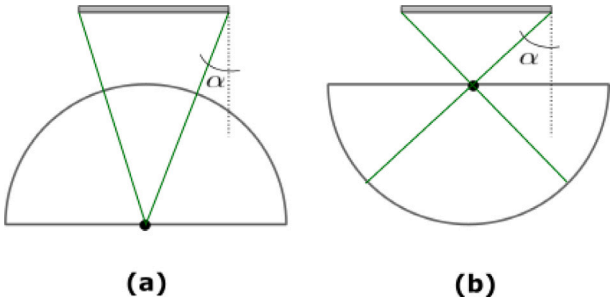

Fig. 6. Deviation of the normal incidence ray (ray that passes through the circle center). (a) Convex case, (b) Concave case.

object coordinates $(0, Ob_2, Ob_3)$ and the image coordinates $(0, Im_2, Im_3)$ are related by [24]:

$$\frac{1}{Im_3} + \frac{1}{Ob_3} = \frac{1}{f} \tag{21}$$

$$Im_2 = -\frac{Im_3}{Ob_3} Ob_2 \tag{22}$$

Eq. (21) is valid only for the so-called paraxial rays, those whose incidence angle θ_{inc} is small enough for the approximation $\theta_{inc} = \sin\theta_{inc}$ to hold.

The cross section of cylindrical mirror whose axis is the x-axis of WCS is a circle in the yz-plane. A ray $\vec{v}_{inc}$ reflected by this mirror can be split as

$\vec{v}_{inc} = \vec{v}_{inc,x} + \vec{v}_{inc,yz}$, being $\vec{v}_{inc,x}$ the component along x-axis, and $\vec{v}_{inc,yz}$ the projection onto yz-plane. The reflected vector is (Fig. 1.b):

$$\vec{v}_{refl} = \vec{v}_{inc} - 2(\vec{v}_{inc}\cdot\hat{n})\hat{n} = \vec{v}_{inc,x} + \vec{v}_{inc,yz} - 2(\vec{v}_{inc,yz}\cdot\hat{n})\hat{n} = \vec{v}_{inc,x} + \vec{v}_{refl,yz} \tag{23}$$

where the relation $\vec{v}_{inc,x}\cdot\hat{n} = 0$ was used, because the normal to the cylinder is always orthogonal to the x-axis. The vector $\vec{v}_{refl,yz}$ is the reflection of $\vec{v}_{inc,yz}$. Therefore, the reflection inside yz-plane can be treated with the circular mirror model. Fig. 8 illustrates the geometry of the problem. The concave case is shown, as it is the one for which this method results more helpful. Nevertheless, the following rationale is valid for both the concave and convex cases. Fig. 8.a show a 3D representation, and Fig. 8.b shows the projection onto yz-plane. It is significant to notice that although the points displayed in Fig. 8.b are projections, we utilized the names of the corresponding 3D points to avoid cluttering the image. A rough outline of the procedure to find the TOF from E_{tx}^{**} to E is the following: a cross section is drawn that contains the receiver E (Fig. 8.a). The emitter E_{tx} is projected onto that plane, and the ray tracing is done in two dimensions (Fig. 8.b), using the circular mirror model, by which we can find the incidence point G (projected onto the plane). The tangent plane at this point can be used to get a mirror image E_{tx}^{**}, such that the TOF can be computed with the distance $\left\|\overline{E_{tx}^{**}E}\right\|$. The step by step description of the procedure:

1. Elements E_{tx} and E are projected onto the yz-plane. We call their projections $proj(E_{tx})$ and $proj(E)$.
2. To define an optical axis, the probe normal $\hat{n}_P$ is also projected onto the yz-plane, and the vertex V is computed as the intersection between the circle and the line from $proj(E_{tx})$ with direction given by $proj(\hat{n}_P)$. The reason to choose this vertex is that the more energetic rays from the emitter have the direction of $\hat{n}_P$.
3. Once the optical axis is defined, the image of E_{tx}^{*} of $proj(E_{tx})$ is computed according to Eq. (21). To this end, the coordinates of $(E_{tx,1}, E_{tx,2})$ of $proj(E_{tx})$ in VCS must be found. Using $(0, V_y, V_z)$ for the WCS coordinates of V as computed in the previous step, the cylinder normal at V gives the direction of the optical axis $\hat{n}_{oa}$ (Fig. 8.b):

$$\left|\hat{n}_{oa}\right|_W = (0, n_{oa,y}, n_{oa,z}) = \pm\left(V_y^2 + V_z^2\right)^{-1/2}(0, V_y, V_z) \tag{24}$$

The coordinate transformation from WCS to VCS is given by:

$$\begin{pmatrix} E_{tx,2} \\ E_{tx,3} \end{pmatrix} = T_{W,V}\begin{pmatrix} E_{tx,y} - V_y \\ E_{tx,z} - V_z \end{pmatrix} \tag{25}$$

$$T_{W,V} = \begin{pmatrix} n_{oa,z} & -n_{oa,y} \\ n_{oa,y} & n_{oa,z} \end{pmatrix} \tag{26}$$

The mirror Eq. (21) can be reformulated to compute the third VCS coordinate $E_{tx,3}^{*}$ of the image as:

$$E_{tx,3}^{*} = \left(\frac{1}{f} - \frac{1}{E_{tx,3}}\right)^{-1} \tag{27}$$

The second component is found with Eq. (22):

$$E_{tx,2}^{*} = -\frac{E_{tx,3}^{*}}{E_{tx,3}} E_{tx,2} \tag{28}$$

4. The coordinates of E_{tx}^{*} in WCS are computed by the inverse transformation:

$$\begin{pmatrix} E_{tx,y}^{*} \\ E_{tx,z}^{*} \end{pmatrix} = T_{W,V}^{-1}\begin{pmatrix} E_{tx,2}^{*} \\ E_{tx,3}^{*} \end{pmatrix} + \begin{pmatrix} V_y \\ V_z \end{pmatrix} \tag{29}$$

5. As show in Fig. 8.b, the ray from $proj(E_{tx})$ reflects at $proj(G)$ and goes to $proj(E)$ through the image E_{tx}^{*}. Thus, point $proj(G)$ can be found by intersecting the line that from $proj(E)$ with direction $\overline{proj(E)E_{tx}^{*}}$
6. The cylinder normal n_G at $proj(G)$ is computed with an equation analogous to (17).

$$\left|\hat{n}_G\right|_W = \pm\frac{(0, G_y, G_z)}{\sqrt{G_y^2 + G_z^2}} \tag{30}$$

and the sign $\pm$ is selected according to the criteria explained in Section 2.1.3

7. The normal n_G defines the tangent plane at G. As shown in Fig. 8.a, the 3D ray from E_{tx} to E is equivalent (same length) to the ray from E_{tx}^{**} to E, where E_{tx}^{**} is the mirror image of E_{tx} by the tangent plane at G. Thus, we compute the TOF as:

$$t_S = \frac{1}{c_1}\left\|\overline{E_{tx}^{**}E}\right\| \tag{31}$$

It is worth to note that unlike E_{tx}^{*}, which is a single point for each emitter, the image E_{tx}^{**} computed at the last step depends on the receiver. As such, it is not a standard mirror image.

The case of a spherical surface is similar but easier. Given E_{tx} and E, the plane that contains these points and the sphere's center should be found. The ray from E_{tx} and E is contained in that plane, thus the problem is treated as the cylindrical one but there is no need of projections.

2.3. Plane wave acquisition

This section presents the calculation of t_S for the case of plane wave emission and the three geometries considered.

2.3.1. Plane surface

A plane wave with direction $\vec{v}_{pw}$ is emitted with delays such that a $t = 0$ the wave front passes through O_P. The wave reflected the xy-plane has direction given by:

$$\vec{v}_{pw}^{*} = \vec{v}_{pw} - 2(\vec{v}_{pw}\cdot\hat{n})\hat{n} \tag{32}$$

and behaves as if emitted from the probe mirror image, thus:

$$t_S = \frac{1}{c_1}\vec{v}_{pw}^{*}\cdot\overline{O_P^{*}E} \tag{33}$$

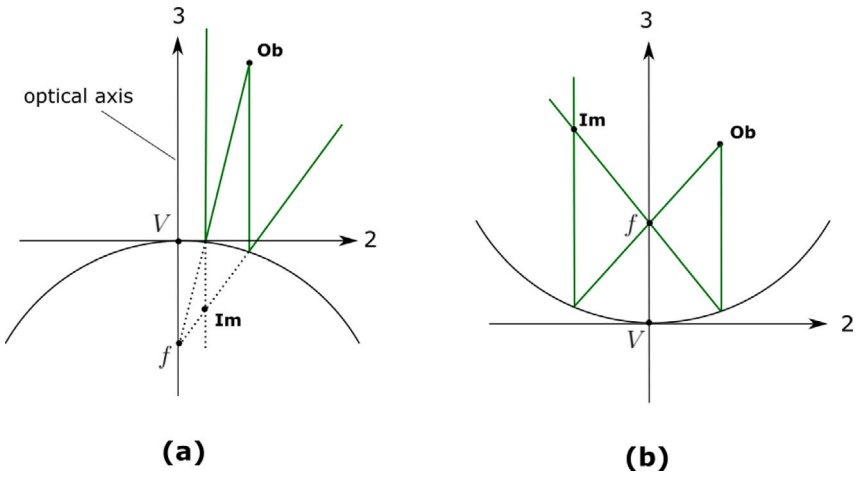

Fig. 7. Geometry of the circular mirror: real and virtual images of an object. (a) Convex case, real image, (b) Concave case, virtual image.

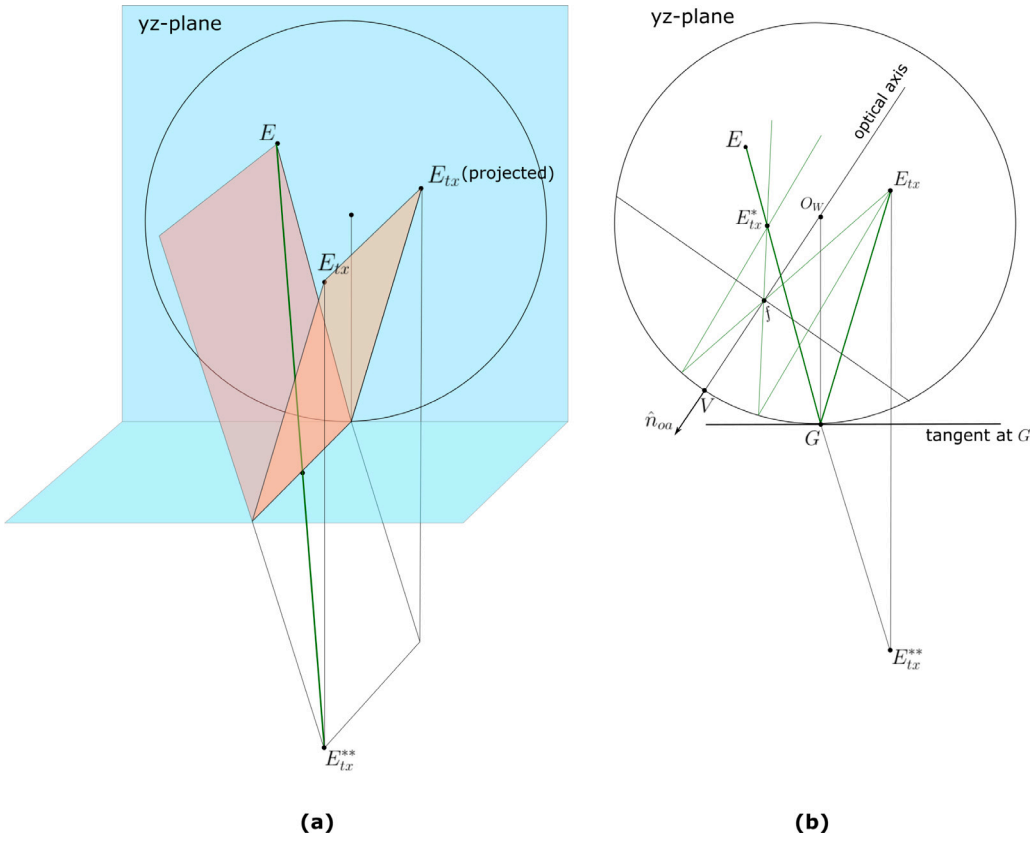

Fig. 8. Cylindrical mirror geometry for the pitch–catch method. (b) 3D view, (b) Projection onto yz-plane, where the circular mirror ray tracing is done according to geometrical optics.

2.3.2. Cylindrical and spherical surfaces

The rationale is very similar to the pitch–catch method described in the preceding section. Fig. 9.a illustrates the geometry involved in the calculations. In this case, instead of a transmitter E_{tx} there is a plane wave with direction given by $\vec{v}_p w$ such that its wave front at time $t = 0$ passes through the probe center O_P. To define an optical axis, the probe normal $\hat{n}_P$ is also projected onto the yz-plane, and the vertex V is computed as the intersection between the circle and the line from $proj(O_P)$ with direction given by $proj(\hat{n}_P)$. The plane wave reflected on the circular mirror converges to a point H on the mirror's focal line (line through f orthogonal to the optical axis. This point H will play the role of E^*_{tx}. As shown in Fig. 9.b, the VCS coordinates of H are given by:

$$(H_2, H_3) = (-f \tan(\beta), f) \tag{34}$$

where $\tan(\beta) = \dfrac{v_{pw,2}}{v_{pw,3}}$.

For each receiving element E, the corresponding $proj(G)$ is found by intersecting the circle. with the line from H that passes through $proj(E)$ (Fig. 9.a). As in the pitch–catch method, the cylinder normal at $proj(G)$ is computed with Eq. (30), and the tangent plane is used to locally reflect the plane wave. The reflected wave vector $\vec{v}^*_{pw}$ is computed with Eq. (23). The probe center mirror image O^*_P created by the tangent plane is computed, and the TOF computed with Eq. (33).

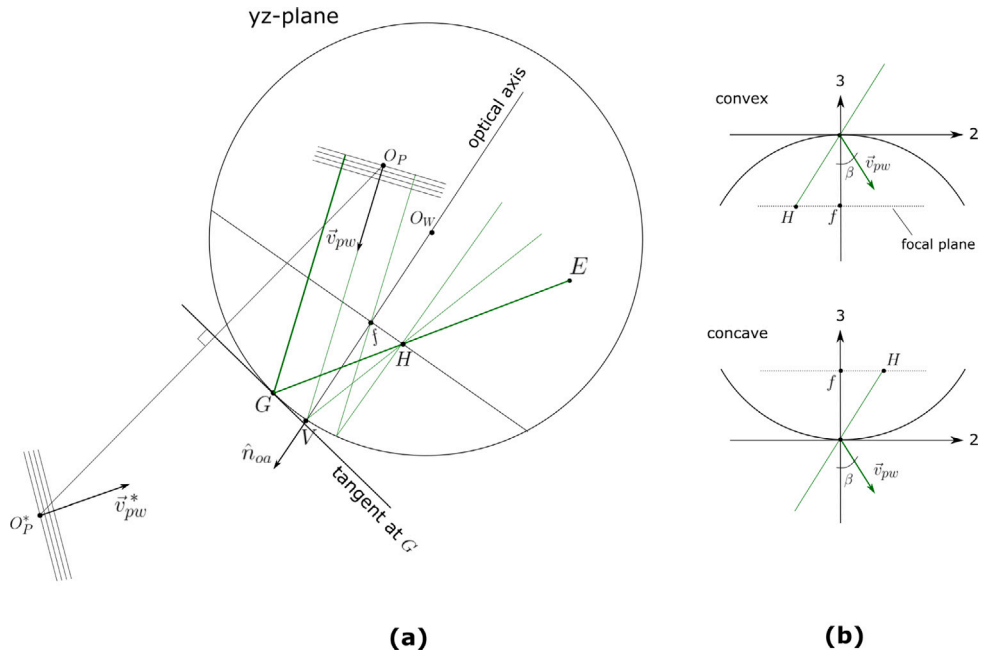

Fig. 9. Circular mirror geometry for the plane wave method.

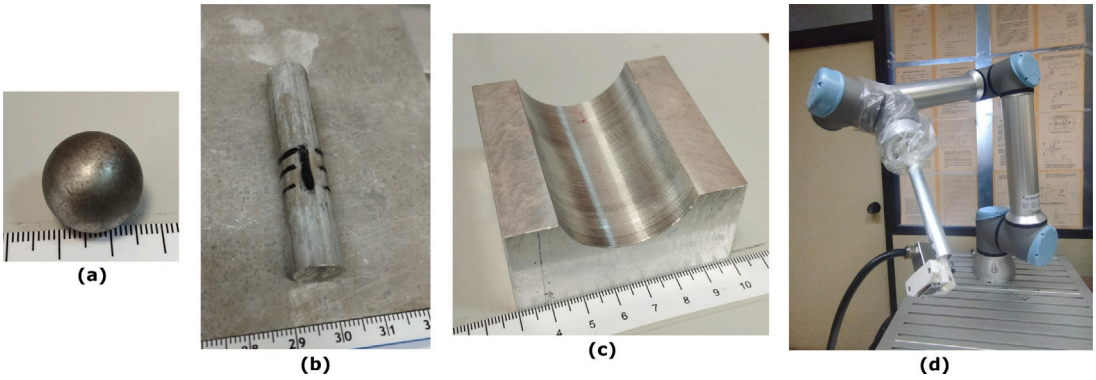

Fig. 10. Test specimens and experimental set-up (a) 9.5 mm radius sphere (b) 6 mm radius rod (c) 40 mm radius concave surface and (d) experimental set-up.

3. Experiments

For validation of the methods proposed in the previous section, a set of experiments were performed using a 3 MHz, 11 × 11 matrix array (Imasonic, France), with 1 mm pitch (square active aperture 11 mm side length). The ultrasound instrument used was a 128 channels full parallel system (DASEL S.L., Spain). Full Matrix Capture (FMC) was used for all acquisitions, as pulse–echo, pitch–catch and plane wave acquisitions can be synthesized from the FMC signals. All the experiments were done in an immersion set up, and a 6-axis collaborative robot (Universal Robots, Denmark) was used for probe positioning.

Four test specimens where used: a flat aluminum plate, a 9.5 mm radius steel sphere (Fig. 10.a), and two cylinders CYL1 (Fig. 10.b) and CYL2 (Fig. 10.c). CYL1 is a 6 mm radius aluminum cylinder that was used to test the convex case. CYL2 is an aluminum block with a 40 mm radius concave cylindrical surface. For the experiments the component was laid onto a flat surface, which was used as a reference plane to measure the probe location and orientation (PLO). In the case of the aluminum plate, the component itself was the reference plane.

In all cases (plane, cylindrical and spherical surfaces) the WCS z-axis was defined orthogonal to the reference plane. For the aluminum plate the specimen surface is the xy-plane (z=0). In the case of the cylindrical surface the cylinder's axis is the x-axis. In the case of the spherical surface the xy-plane is parallel to the reference plane and the coordinate origin is at the sphere's center. In order to measure the nominal PLO the following procedure was used:

1. The 6 degrees of freedom used by the robot are $(x, y, z, \theta_x, \theta_y, \theta_z)$. An initial PLO is defined $PLO_0 = (0, 0, z_0, 0, 0, 0)$. To physically set this PLO_0 the probe face must be oriented parallel to the reference plane. This is achieved by acquiring the pulse–echo A-scan of the probe corner elements. The probe is rotated until the surface echo TOF is equal in the four signals. In this way the angles θ_x, θ_y are set to zero.
2. Once the probe face is orthogonal to the z-axis, it is located at an arbitrary height above the reference plane, and then gently moved towards it until contact. The contact condition is detected by the robot's force sensor. The amount of the displacement is z_0 in the plane surface case, and $z_0 - h$ in the cylindrical and spherical cases, where h is the height of the center relative to the reference plane, which is a known geometrical dimension of the component.
3. For the plane surface, any position can be defined as $(x = 0, y = 0)$. In the cylindrical case, to set $y = 0$ and $\theta_z = 0$ it is needed to center the probe above the cylinder. This is achieved by gently displacing and rotating the cylinder in order to set

Table 1
Variables changed in each experiment.

	Exp1	Exp2
Plane	θ_x, θ_y	z, θ_x
Sphere	x, y	x, z
Cylinder	θ_y, θ_z	y, z

the same surface echo TOF in the four corner element A-scans, which means that the probe is centered on the cylinder axis and symmetric about the xz-plane. The same method is used to center the probe above the sphere, which sets $(x = 0, y = 0)$

4. Starting from PLO_0, relative motions are preformed with the robotic arm. Therefore, the target values are taken as the $(x, y, z, \theta_x, \theta_y, \theta_z)$ measurements.

It is worth to mention that although the robotic arm has a 0.05 mm repeatability, the PLO measurements are affected by a systematic error introduced in the procedure to set the PLO_0 and in the measurement of the geometrical dimensions of the specimens. For example, when adjusting PLO_0 to set $y = 0$ for the cylinder case, the four A-scan signals cannot be perfectly aligned to get the same surface echo TOF. Thus, some small offset in y is to be expected. Additionally, the height h of the cylinder axis relative to the reference plane, which is measured by mechanical means, is subject to an error that propagates to z_0.

Furthermore, there is another systematic error source: to keep O_P fixed, the robot's Tool Center Point (TCP) must be correctly set. To this end, the O_P coordinates relative to the robot tool flange must be known. This depends on the probe holder device and is subject to measurement error. Thus, when rotating the probe, O_P will move on the surface of sphere whose radius is the TCP error.

For all the FMC acquisitions, the surface echo TOF $t_S(i)^*$ was measured by threshold crossing. To achieve this, we employed the signal envelope and picked the first point that exceeded the threshold, which was chosen relative to background noise. For each signal, a T_{win} width window starting at the threshold crossing time $t_S(i)^*$ was used to compute a feature $w(i)$ that characterizes the amplitude of the detected surface echo:

$$w(i) = \max_{0 \le \tau \le T_{win}} a(i, t_{thr} + \tau) \tag{35}$$

where $a(i, t)$ is the element i signal envelope. These features are the weights used in the cost Eq. (4), to reduce the impact of low amplitude signals (more affected by noise) during the optimization process.

The pitch–catch methods was applied in all cases using 9 emitter elements: those with indexes (1, 1), (5, 1), (1, 5), (9, 1), (1, 9), (5, 9), (9, 5), (9, 9), (5, 5). For the sphere and for CYL1, the receiving sub-aperture was 3 × 3 elements, centered in the emitter.

The plane wave method was applied with a single emission: a 0° plane wave relative to the probe face normal. If we suppose no prior knowledge of the PLO, then this plane wave direction is a natural choice. The plane wave acquisition was synthesized from the FMC data.

For each specimen, two experiments Exp1 and Exp2 were done. In each experiment PLO was varied in two of its degrees of freedom and an FMC was acquired for each PLO. Table 1 summarizes the degrees of freedom varied for each experiment.

4. Results

This section presents the results of the methods developed in Section 2 when applied to the four test specimens.

Table 2
Error statistics (**std**:standard deviation) for the two experiments with the plane surface. In the case of the plane wave method, the statistics where computed excluding angles larger than 5°.

PLANE		pulse-echo			pitch-catch			plane wave		
		mean	std	max	mean	std	max	mean	std	max
Exp1	z (mm)	−0.25	0.09	0.36	−0.23	0.08	0.33	−0.27	0.03	0.3
	θ_x (°)	−0.25	0.09	0.46	−0.26	0.07	0.46	−0.47	0.3	1.04
	θ_y (°)	−0.01	0.14	0.35	−0.01	0.12	0.35	−0.17	0.25	0.76
Exp2	z (mm)	−0.21	0.1	0.35	−0.16	0.06	0.25	−0.19	0.03	0.24
	θ_x (°)	−0.19	0.17	0.88	−0.25	0.09	0.42	−0.53	0.46	1.58
	θ_y (°)	0.10	0.13	0.51	0.12	0.06	0.21	0.07	0.04	0.16

4.1. Plane surface

Figs. 11 and 12 show the fitted PLO parameters for the aluminum plate Exp1 and Exp2 respectively. Abcissas correspond to nominal values of one degree of freedom. The other degree of freedom is indicated by colors in the legend. The ordinates correspond to the estimated values. Table 2 contains overall error statistics. It is observed in Figs. 11 and 12 that the pulse–echo and pitch–catch methods provide very similar results: in a general view both perform well in measuring both z and the angles, but z values are systematically lower than the target value by an amount of about 0.2 mm (as can be seen in Table 2). This systematic error is related to the fact that ultrasonic TOF absolute distance measurement is a difficult task, greatly affected by the method used to measure the pulse arrival time [19]. Errors in $t_S(i)^*$ directly affect z. However, the amount of z displacements (2 mm nominal value) in Exp2 is accurately measured: the mean value is 2 mm (negligible systematic error) and the standard deviation 0.02 mm. On the other hand, the plane wave methods fails for angles larger than 5°, and has larger errors for angle estimation (Table 2). This is to be expected: as the angle between the plane wave direction and the surface normal gets large, only a few reflected rays impinge on the probe aperture causing most of the array elements to receive very low acoustic energy. However, as can be observed in Fig. 12, z values are still correctly estimated for some PLOs, even for cases in which θ_x presents a large error, and z displacements are as accurate as with the pulse–echo and pitch–catch methods. Thus, for an application where angles are expected to be close to zero, the plane wave method might be a good choice, considering that it uses a single emission.

4.1.1. Spherical surface

Figs. 13 and 14 show the fitted PLO parameters for the steel sphere Exp1 and Exp2 respectively. Table 3 contains overall error statistics. It is observed that the three methods have a good performance. Coordinates x and y are estimated in all cases with a precision (standard deviation) of less that 0.1 mm and about 0.1 mm systematic error probably caused by an error in the PLO_0 setting. Coordinate z, as with the plane surface case, shows the same type of systematic error: about 0.3 mm in the pulse–echo and pitch–catch methods. In the plane wave case this systematic error shows a very different behavior than the other two methods, as can be observed in Fig. 13. While for pulse–echo and pitch–catch the estimated z is almost constant as y changes, in the plane wave case z estimation shows a systematic increase as y departs from 0. This is consistent with the limitations of the circular mirror approximation used in the model: as the probe center departs from the z-axis, the optical axis forms a larger angle with the 0° emitted plane wave and the paraxial approximation gets less accurate. In relation to z displacement errors, the same accuracy and precision as in the plane surface case are obtained for the three methods: a negligible systematic error and 0.02 mm standard deviation.

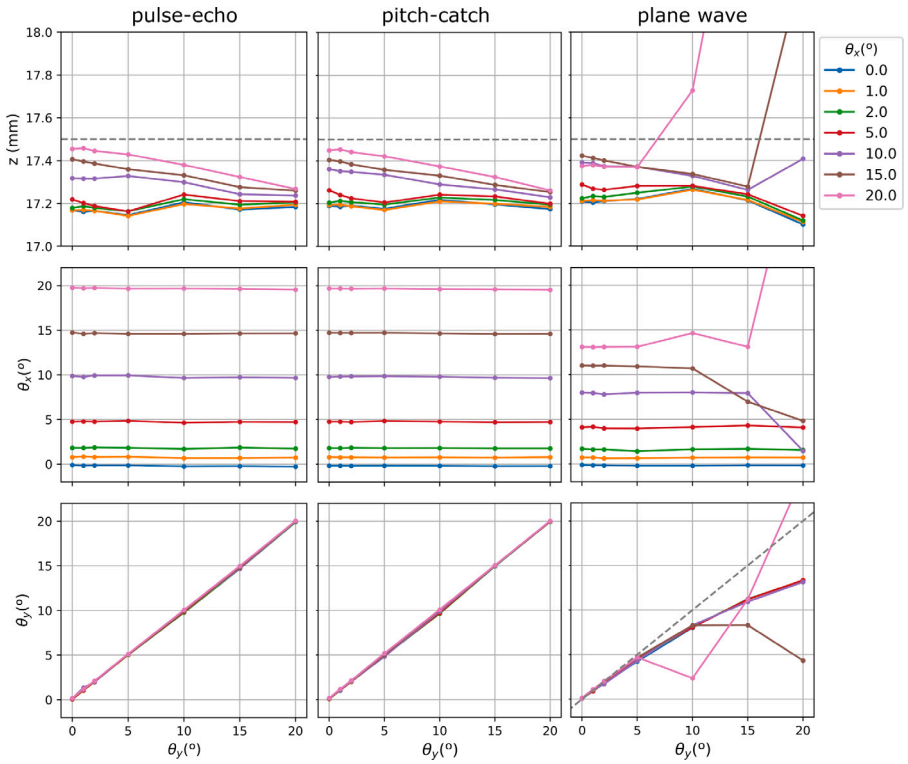

Fig. 11. Plane surface Exp1 results. The abscissas corresponds to the nominal θ_y values, and the ordinates to the fitted values. Nominal z_0 is 17.5 mm (dashed line).

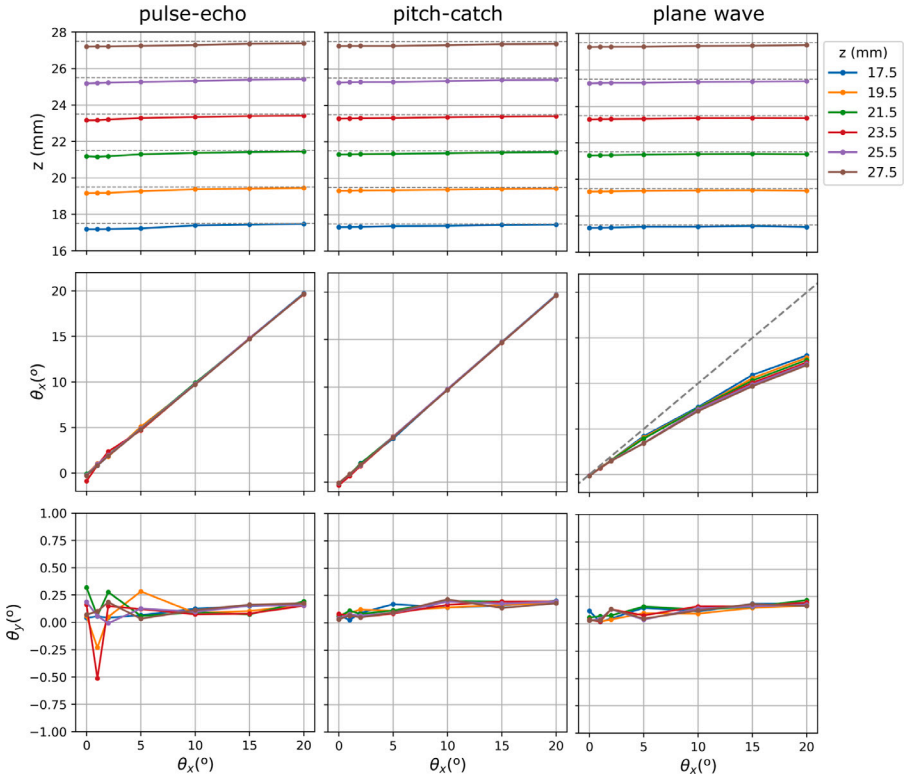

Fig. 12. Plane surface Exp2 results. The abscissas corresponds to the nominal θ_x values, and the ordinates to the fitted values. The horizontal dashed lines in the z plots indicate de nominal values.

4.1.2. Cylindrical surface

CYL1, convex surface. Figs. 15 and 16 show the fitted PLO parameters for CYL1 Exp1 and Exp2 respectively. Table 4 contains overall error statistics. It is observed that, as in the previous cases, pulse–echo an pitch–catch methods provide very similar results, and that the plane wave methods starts to fail for θ_y larger than 5° (absolute value). The systematic error in z coordinate is again observed, around 0.5 mm in this case. Fig. 15 shows a trend in y and z. As this trend shows an

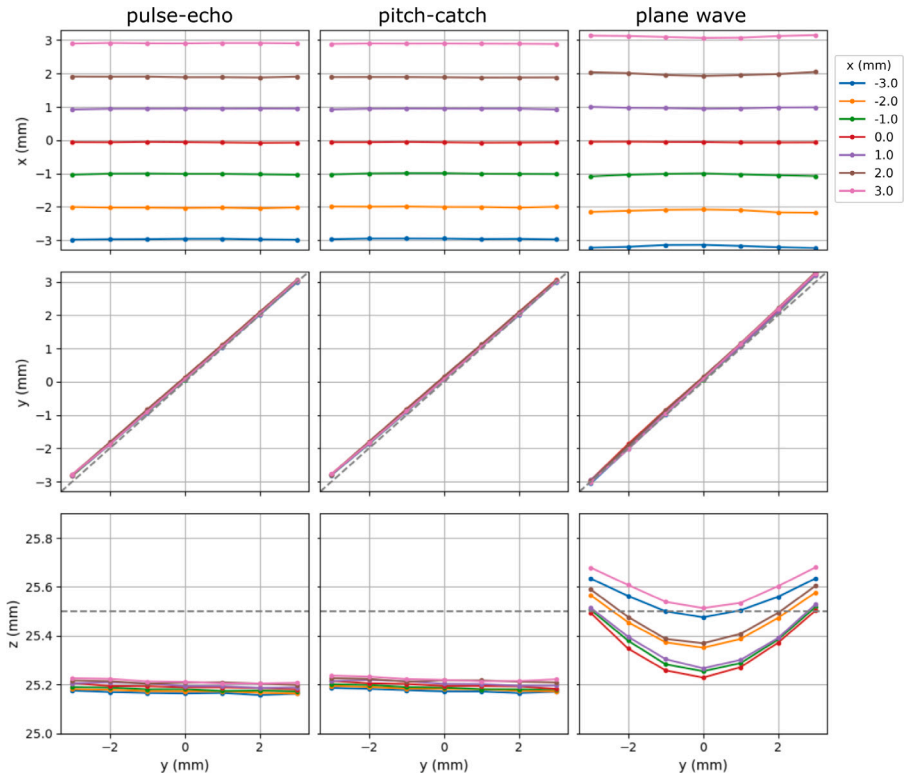

Fig. 13. Spherical surface Exp1 results. The abscissas corresponds to the nominal y values, and the ordinates to the fitted values. Nominal z_0 is 25.5 mm (dashed line).

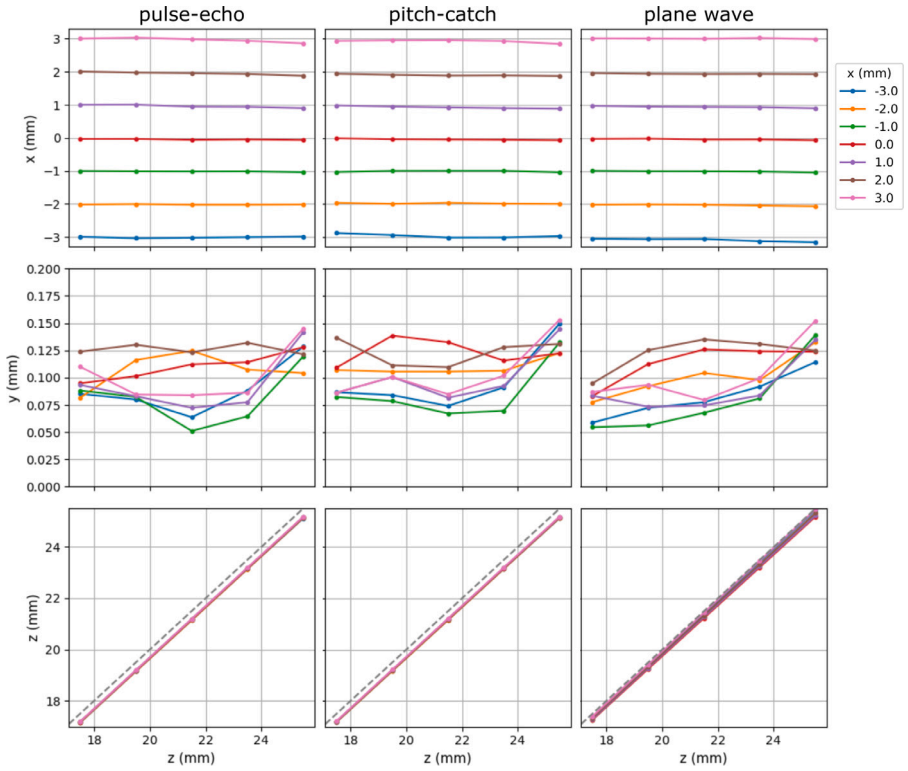

Fig. 14. Spherical surface Exp2 results. The abscissas corresponds to the nominal z values, and the ordinates to the fitted values. Nominal y is 0 mm.

asymmetric effect about the xz-plane, we think this is mainly due to an inexact PLO_0 with a small offset in coordinate y. In fact, the measured y values show a positive mean offset (Fig. 15). Additionally, a TCP configuration error might have such an asymmetric trend effect.

CYL2, concave surface. In this case the methods applied are pitch–catch with the complete receive aperture, and plane wave. As explained in Section 2.1.2 pulse–echo signals in a concave case might suffer from a low angular sensitivity effect and the pulse–echo method in fact failed

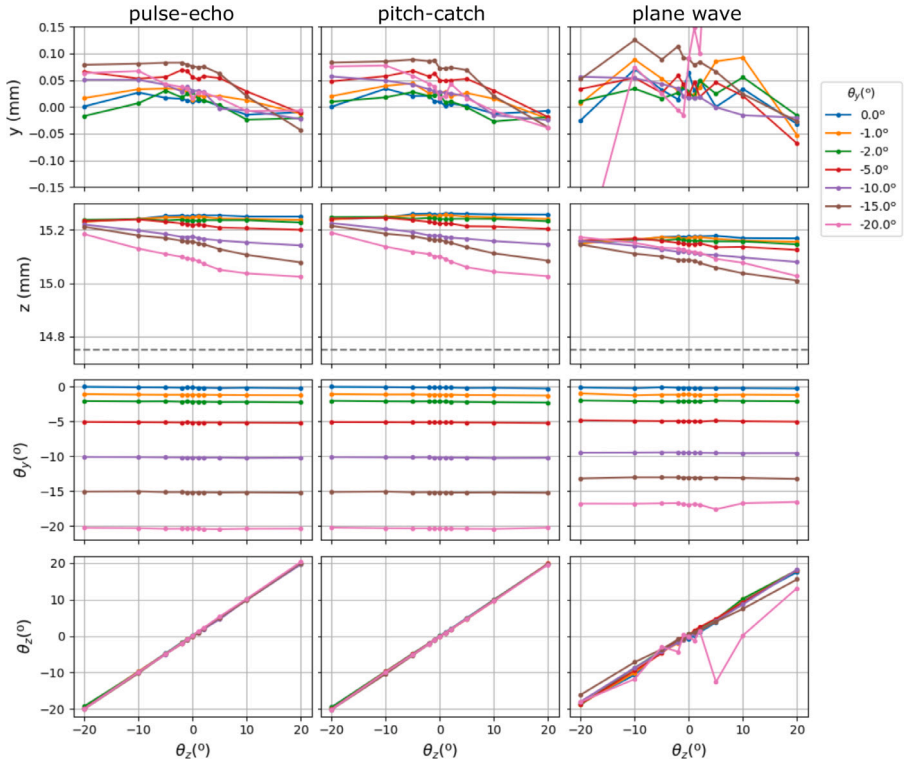

Fig. 15. CYL1 Exp1 results. The abscissas corresponds to the nominal θ_y values, and the ordinates to the fitted values. Nominal z_0 is 14.75 mm (dashed line).

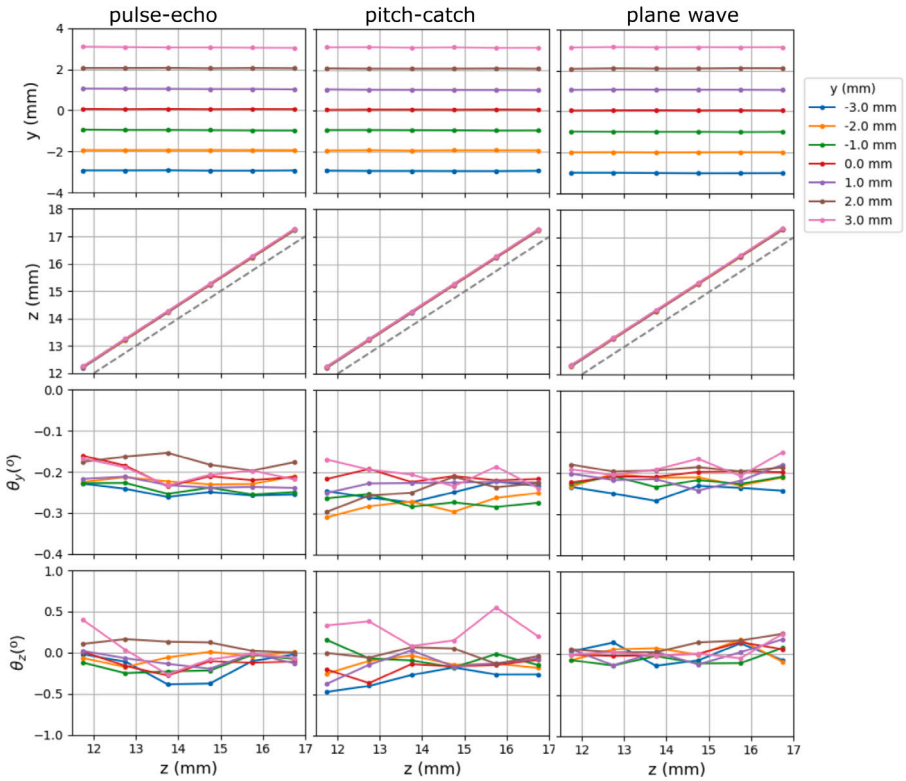

Fig. 16. CYL1 Exp2 results. The abscissas corresponds to the nominal z values, and the ordinates to the fitted values. Nominal angles are $\theta_y = 0°$ and $\theta_z = 0°$.

when tried with CYL2. Figs. 17 and 18 show the fitted PLO parameters for CYL2 Exp1 and Exp2 respectively. Table 5 contains overall error statistics. The pitch–catch method shows good performance but as z gets closer to the cylinder center errors increase, as can be seen in Fig. 18. This is related to the fact that when a source element is located on a diametrical line of a circular mirror, its mirror image is also located in that same line, as can be derived from (21). Thus, acoustic energy gets concentrated in few array elements. This causes $w(i)$ to be very low

Table 3
Error statistics for the two experiments with the spherical surface.

SPHERE		pulse-echo			pitch-catch			plane wave		
		mean	std	max	mean	std	max	mean	std	max
Exp1	x (mm)	−0.05	0.04	0.12	−0.05	0.05	0.12	−0.05	0.09	0.24
	y (mm)	0.10	0.06	0.22	0.11	0.07	0.23	0.11	0.08	0.29
	z (mm)	−0.31	0.02	0.34	−0.3	0.02	0.33	−0.04	0.12	0.27
Exp2	x (mm)	−0.03	0.04	0.14	−0.03	0.06	0.15	−0.04	0.04	0.16
	y (mm)	0.10	0.02	0.15	0.11	0.02	0.15	0.10	0.03	0.15
	z (mm)	−0.33	0.02	0.38	−0.32	0.02	0.37	−0.18	0.08	0.32

Table 4
Error statistics for the two experiments with CYL1. In the case of the plane wave method, the statistics where computed excluding $\theta_y > 15°$.

CYL1		pulse-echo			pitch-catch			plane wave		
		mean	std	max	mean	std	max	mean	std	max
Exp1	y (mm)	0.03	0.03	0.08	0.03	0.03	0.09	0.03	0.04	0.13
	z (mm)	0.44	0.06	0.50	0.45	0.06	0.51	0.39	0.04	0.43
	θ_y (°)	−0.22	0.09	0.47	−0.21	0.08	0.44	0.32	0.75	1.97
	θ_z (°)	0.06	0.18	0.79	−0.09	0.18	0.48	0.02	1.27	4.45
Exp2	y (mm)	0.06	0.02	0.1	0.06	0.02	0.1	0.06	0.02	0.1
	z (mm)	0.49	0.02	0.52	0.50	0.02	0.53	0.5	0.02	0.53
	θ_y (°)	−0.22	0.03	0.26	−0.24	0.03	0.31	−0.24	0.03	0.31
	θ_z (°)	−0.07	0.14	0.4	−0.08	0.2	0.56	−0.08	0.2	0.56

Table 5
Error statistics for the two experiments with CYL2. In the case of the plane wave method, the statistics where computed excluding $\theta_y > 5^{circ}$ and $z < 5$ mm.

CYL2		pitch-catch			plane wave		
		mean	std	max	mean	std	max
Exp1	y (mm)	0.03	0.07	0.2	0.02	0.07	0.17
	z (mm)	−0.49	0.06	0.69	−0.48	0.01	0.53
	θ_y (°)	−0.34	0.07	0.52	−0.02	0.26	0.48
	θ_z (°)	−0.35	0.1	0.7	0.03	0.93	3.39
Exp2	y (mm)	−0.02	0.08	0.25	−0.0	1.26	5.66
	z (mm)	−0.44	0.03	0.5	−0.48	0.11	0.96
	θ_y (°)	−0.03	0.06	0.23	0.04	0.14	0.86
	θ_z (°)	−0.04	0.55	1.79	−0.28	1.56	6.23

for many elements and very high for the few elements where acoustic energy is concentrated, possibly leading to a bad least squares fitting. A similar effect is observed in Fig. 18 for the plane wave method. In this case there is another detrimental effect: as y gets away from 0 the mean incidence angle of the 0° plane wave increases and the reflected wave is directed away from the aperture. Additionally, Fig. 17 shows that the plane wave method, as with CYL1, starts to fail for larger θ_y values. To sum up, the result is that the plane wave method has a limited range of application. As in the plane surface case, it might be useful in some case where no large deviations are expected from a PLO inside the working range. At last, it is observed in Figs. 17 and 18 the systematic error in the z coordinate common to all the methods and test specimens analyzed in this work, which, as mentioned before, is a problem inherent to TOF measurements. Furthermore, these kind of constant small displacements in a single direction do not have a great impact in image quality, as they act essentially as a common offset in the TOF estimation of all elements.

4.1.3. TFM imaging with the estimated PLO

CYL1 test specimen has 3 bottom-drilled holes in its xz plane (Fig. 19.a), having 3, 6, and 9 mm depth. In this section we present CYL1 TFM images (Fig. 19 b to e) computed using the PLO estimated with the pulse–echo method. Four D-scans are presented, corresponding to four different PLOs taken from the experiments described in Section 3. Fig. 20 shows a 3D view of the four PLOs.

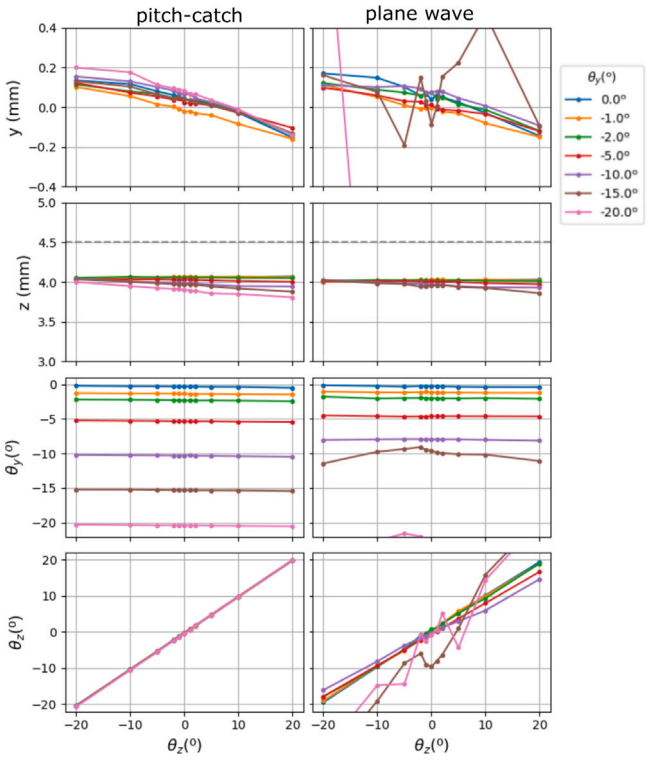

Fig. 17. CYL2 Exp1 results. The abscissas corresponds to the nominal θ_y values, and the ordinates to the fitted values. Nominal z_0 is 4.5 mm (dashed line).

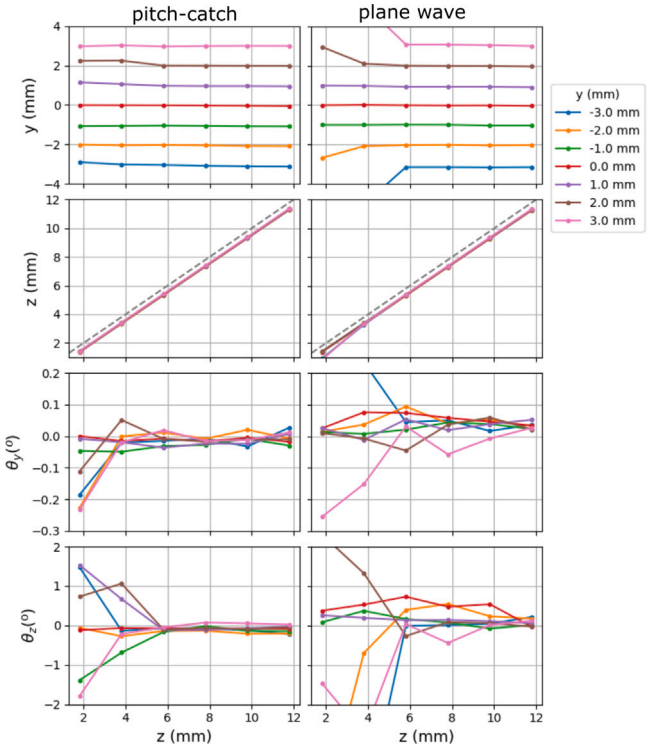

Fig. 18. CYL2 Exp2 results. The abscissas corresponds to the nominal z values, and the ordinates to the fitted values. Nominal angles are $\theta_y = 0°$ and $\theta_z = 0°$.

We can observe in Figs. 19 b to e how the 3 holes are always clearly imaged and their positions do not show significant differences, despite the probe position is significantly changed between them. There are

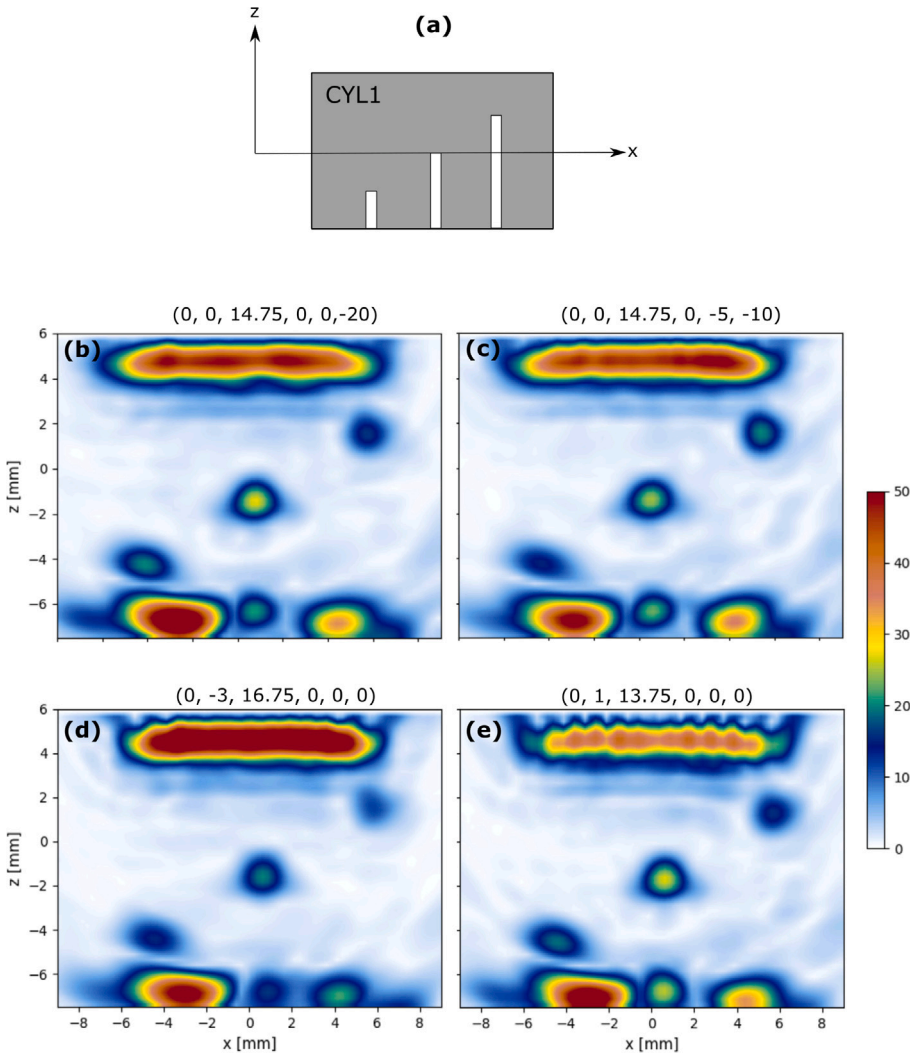

Fig. 19. CYL1 D-scan TFM images computed with the estimated PLO. The $(x, y, z, \theta_x, \theta_y, \theta_z)$ values are shown above of each D-scan, in mm and degrees. (a) Schematic of CYL1 bottom-drilled holes (c)–(e) D scans corresponding to four different PLOs.

variations in the amplitudes of the indications, which are expected due to the effects of angular sensitivity and refraction angles, both changing when array elements move.

5. Discussion

The results presented in the previous section show that the pulse–echo and pitch–catch methods achieve similar performances. Their errors in the measurement of (x,y) coordinates have a less than 0.5 mm average value and less than 0.1 mm standard deviation for the three tested geometries. z coordinate presents a larger systematic error (about 0.5 mm in the worst case for the performed experiments), but z displacements have negligible systematic error and 0.02 mm standard deviation. Angular error have less than 1° average and standard deviation. These results are valid up to the 20° maximum angle applied in the experiments.

For FMC acquisition, the available signals allow the application of both (pulse–echo and pitch–catch) methods. In this case, pulse–echo is preferable due to its simpler calculations. However, for Phased Array (PA) applications, surface estimation and imaging are done in two sequential stages. Firstly a set of emissions is used for surface estimation, and then focal laws can be computed for the imaging emissions. In this case, a pitch–catch acquisition is faster than pulse–echo, because significantly fewer emissions are needed (9 instead of 121 in our experiments). Nevertheless, in the case of complete receive aperture, more signals are needed (1089 instead of 121 for the example), and calculations are more complex. Therefore, depending on data transfer rates available and the degree of optimization in the algorithm implementation, pulse–echo might result faster than pitch-catch. Regarding the plane wave method, its application resulted more restrictive than the other two, because it starts to fail as angles increase. The method showed a good performance (similar to pulse–echo and pitch-catch) up to 5° angles. In this range a single plane wave emission is a good choice for PA applications, but again this depends on the degree of optimization in the algorithm implementation, because more mathematical operations are needed for the spherical mirror model. Even so, for the concave surface case pulse–echo might be not applicable.

The maximum working angle for the plane wave method can be estimated as a function of the probe aperture and height relative to the surface. This depends on the geometry and we derived the equation for a plane surface in Appendix, where it is shown that for rotation around either x or y axis, the maximum angle is approximately $3\frac{D}{z}$ degrees for a width D aperture and height z.

Finally we will discuss how TFM images would be affected if PLO is not measured, and instead a nominal PLO_{nom} is used for TOF calculations. We will use CYL1 as example and suppose a situation in which the probe is by set-up design nominally positioned with PLO_{nom} =

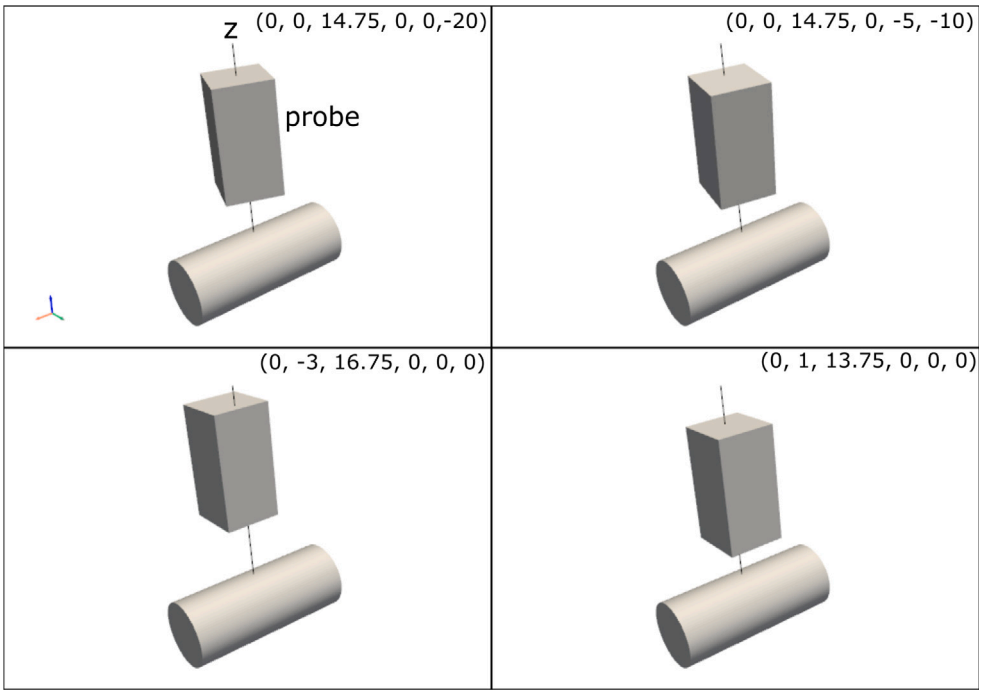

Fig. 20. 3D view of the 4 PLOs for which D-scans are shown in Fig. 19. The $(x, y, z, \theta_x, \theta_y, \theta_z)$ values are shown above of each PLO, in mm and degrees.

$(0, 0, 15, 0, 0, 0)$. Fig. 21 shows TFM D-scan images for two PLOs, using the nominal PLO (Figs. 21.a and 21.c) and the PLO measured with the pulse–echo method proposed (Figs. 21.b and 21.d). It is observed that if no PLO correction is applied the images are significantly distorted. However, the application of the purposed method achieves a clear improvement. The experiments presented were performed with a 3 MHz probe. For higher frequencies, we would expect the same TOF errors to have a greater impact on image distortion, and therefore, correcting the PLO would become more important. Experimental testing of this hypothesis is a potential subject for future work.

Finally, we will discuss how TFM images would be affected by positioning errors if PLO is not measured and, instead, a nominal PLO_{nom} is used for TOF calculations. We will use CYL1 as example, assuming that the probe is located by design at $PLO_{nom} = (0, 0, 14.75, 0, 0, 0)$, but positioning errors are present. Two cases will be analyzed: A slight movement below 1° and 1 mm in all axis with $PLO_1 = (0, 0.99, 15.22, 0, 0.22, 0.47)$ and a larger misalignment with $PLO_2 = (0, 0.05, 15.23, 0, -5.13, -9.86)$.

Fig. 21 shows TFM D-scan images for the two cases, using the nominal PLO (Figs. 21.a and 21.c) and the PLO measured with the proposed pulse–echo method (Figs. 21.b and 21.d). It is observed that if no PLO correction is applied, the images are significantly distorted. Even in the case of a small misalignment PLO_1 the amplitude of the defects is reduced, which would lead to missing some of them if a detection threshold is applied. For larger position deviations like in PLO_2, besides the amplitude reduction because of wrong focusing delays, the image displacement can take defects out of the measuring gates, or even out of the image region. Furthermore, the position of the defects with regard to the global coordinate system will be wrong.

It is worth to remark that images 21.b and 21.d are obtained solely from the received ultrasonic data, without requiring any external mean for measuring or correcting the probe position. This is the principal contribution of the proposed method.

The experiments in this work were performed with a 3 MHz probe. For higher frequencies, we would expect the same PLO errors to have a greater impact on the image quality, because the same time-shift implies a larger misalignment with regard to the wavelength, leading to a more destructive interference. Therefore, in principle, correcting the PLO errors would become more necessary for higher frequency arrays.

With regard to the performance of the proposed method, we do not foresee any degradation apart from that relative to working at higher frequencies, like lower signal-to-noise-ratio or higher element directivity. In fact, interface detection and PLO estimation would be probably more precise using shorter pulses resultant from higher frequency arrays. Experimental testing of this hypothesis is a potential subject for future work.

6. Conclusions

In this work we have presented some methods for 2D array surface detection and estimation of the probe location and orientation. In particular, the methods developed are applicable to the immersion testing of components with plane, cylindrical or spherical surfaces. These elementary surfaces are very common in industrial and structural components for which 3D ultrasound imaging with 2D arrays can provide a solution for some problems associated with linear arrays, such as low resolution in the passive direction and misalignment which refract the beam out of the image plane.

The developed methods use three types of acquisitions: pulse–echo, pitch–catch and plane wave. They are based in surface echo time of flight measurements and its fitting by a forward model.

We have shown experiments with the three types of geometry concluding that the pulse–echo and pitch–catch methods perform similarly, with (x,y) coordinate errors having a less than 0.5 mm average value and less than 0.1 mm standard deviation. z coordinate presents a larger systematic error (about 0.5 mm in the worst case for the performed experiments) while the z displacements show negligible systematic error and 0.02 mm standard deviation. Angular errors have less than 1° average and standard deviation.

On the other hand the plane wave method, despite having a faster acquisition time (single emission), has shown to have a limited angular range of application, and slightly larger errors.

Moreover, a 3D TFM imaging example was shown for a cylindrical component, in which three bottom drilled holes are correctly detected for wide a range of PLOs, using the automatic surface and PLO detection proposed methods.

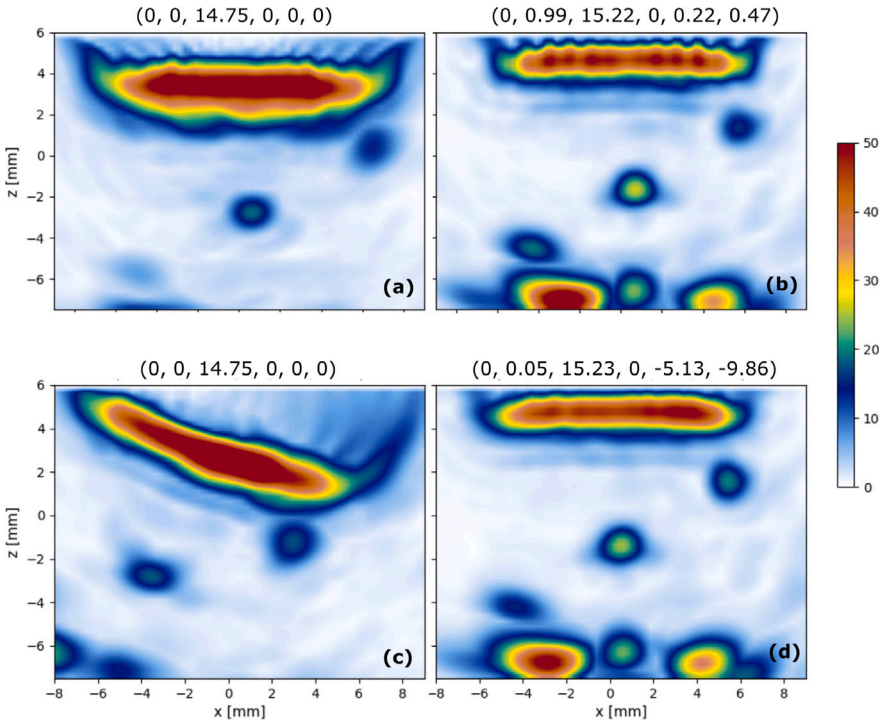

Fig. 21. Examples showing the effect of using an incorrect PLO for image computation. The PLO used in each case is indicated above each image, in mm and degrees. (a) and (c) A nominal PLO is used (no correction), (b) and (d) The PLO measured by the pulse–echo method proposed is used.

CRediT authorship contribution statement

Guillermo Cosarinsky: Conceptualization, Methodology, Software, Formal analysis, Writing, Visualization. **Jorge F. Cruza:** Conceptualization, Methodology, Writing. **Mario Muñoz:** Conceptualization, Software. **Jorge Camacho:** Conceptualization, Methodology, Writing, Supervision.

Declaration of competing interest

The authors declare that they have no known competing financial interests or personal relationships that could have appeared to influence the work reported in this paper.

Data availability

Data will be made available on request.

Acknowledgments

This research was supported by the projects PDC2022-133504-I00 founded by MCIN/AEI/10.13039/501100011033 (Spain) and "Next Generation EU"/PRTR (European Union), by the fellowship PRE2019-088602 founded by MCIU (Spain) and by the project PID2022-143271OB-I00, founded MCIN/AEI /10.13039/501100011033/FEDER, UE

Appendix. Estimation of the maximum working angle for the plane wave method

In this section we derive a method for estimation of the plane wave method maximum working angle. The derivation is done for the plane surface case, considering for simplicity a rotation only about the y-axis. For a cylindrical surface the equation might be used in an tentative way if radius is not too small relative to the probe aperture. Fig. 22 shows a 2D section where the reflected plane wave is plotted as a light green region. The probe has aperture D in the x direction and its center is at height z. The part of the aperture highlighted in green and starting at point B is where plane wave energy is received. As this part decreases the plane wave model will start to fail. Thus, we postulate that the working range corresponds to $B_x < k\frac{D}{2}$ where k will be empirically chosen and is such that $-1 < k < 1$. Between A and B some energy is received from side lobes, but it does not propagate as a plane wavefront. Point B is found as the intersection of the probe aperture with the reflected ray (red line in Fig. 22) from point A. The resulting equation is:

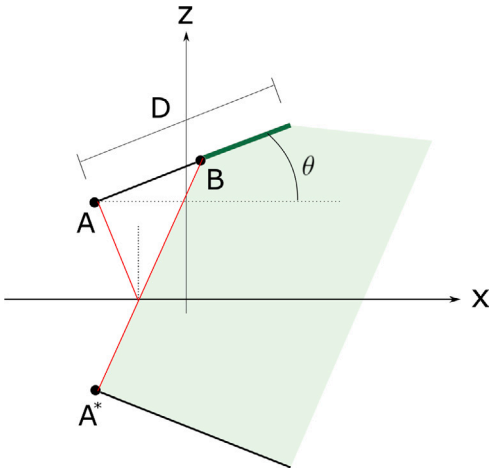

Fig. 22. Schematic for the estimation of the maximum working angle for the plane wave method.

$$B_x = \left(2z\sin(\theta) - \frac{D}{2}\right)\left(\cos(\theta)(1-\tan(\theta)^2)^{-1}\right) \tag{36}$$

Up to first order in θ Eq. (36) can be approximated as:

$$B_x = \left(2z\theta - \frac{D}{2}\right) \tag{37}$$

Therefore, the maximum angle is:

$$\theta_{max} = (1-k)\frac{D}{4z} \tag{38}$$

To chose a value for k we look at Fig. 12, where we can observe that $\theta_{max} \approx 5°$ for every tested z value. If we replace the z average value (22.5 mm) and the 10 mm probe aperture in (37), we get $k \approx 0.8$. Thus, θ_{max} in degrees is given by:

$$\theta_{max} \approx 3\frac{D}{z} \tag{39}$$

The Eq. (39) is a rough semi-empirical approximation that should be used only in a orientative way.

References

[1] Drinkwater BW, Wilcox PD. Ultrasonic arrays for non-destructive evaluation: A review. NDT E Int 2006;39(7):525–41. http://dx.doi.org/10.1016/j.ndteint.2006.03.006, URL https://www.sciencedirect.com/science/article/pii/S0963869506000272.

[2] Schmerr LW. Fundamentals of ultrasonic phased arrays. Solid Mechanics and Its Applications. vol. 215, 2015, p. 1–389.

[3] Braconnier D, Takahashi M. 2D arrays and volume focusing combined inspection technique. In: 17th world conference on nondestructive testing. 2008, p. 25–8, URL http://www.ndt.net/article/wcndt2008/papers/625.pdf.

[4] Huang Q, Zeng Z. A review on real-time 3D ultrasound imaging technology. BioMed Res Int 2017;2017(April). http://dx.doi.org/10.1155/2017/6027029.

[5] Reverdy F, Le Ber Eddyfi L, Mahaut S, Dubois P, Le Ber L, Roy O. Advanced matrix phased array settings for inspection. 2008, p. 25–8, URL https://www.researchgate.org/publication/229035105.

[6] Waltham DA. Two-point ray tracing using Fermat's principle. Geophys J Int 1988;93(3):575–82. http://dx.doi.org/10.1111/j.1365-246X.1988.tb03883.x, arXiv:https://academic.oup.com/gji/article-pdf/93/3/575/1902054/93-3-575.pdf.

[7] Sutcliffe M, Weston M, Charlton P, Donne K, Wright B, Cooper I. Full matrix capture with time-efficient auto-focusing of unknown geometry through dual-layered media. Insight, Non-Destr Test Cond Monit 2013;55(6):297–301. http://dx.doi.org/10.1784/insi.2012.55.6.297.

[8] Robert S, Calmon P, Calvo M, Le Jeune L, Iakovleva E. Surface estimation methods with phased-arrays for adaptive ultrasonic imaging in complex components. AIP Conf Proc 2015;1650(2015):1657–66. http://dx.doi.org/10.1063/1.4914787.

[9] Matuda MY, Buiochi F, Adamowski JC. Experimental analysis of surface detection methods for two-medium imaging with a linear ultrasonic array. Ultrasonics 2019;94(August 2018):50–9. http://dx.doi.org/10.1016/j.ultras.2018.12.004.

[10] Chen Q, Xie Y, Cao H, He Z, Wang D, Guo S. Ultrasonic inspection of curved structures with a hemispherical-omnidirectional ultrasonic probe via linear scan SAFT imaging. NDT E Int 2022;129(February):102650. http://dx.doi.org/10.1016/j.ndteint.2022.102650.

[11] Camacho J, Cruza JF, Brizuela J, Fritsch C. Automatic dynamic depth focusing for NDT. IEEE Trans Ultrason Ferroelectr Freq Control 2014;61(4):673–84. http://dx.doi.org/10.1109/TUFFC.2014.2955.

[12] Holmes C, Drinkwater B, Wilcox P. The post-processing of ultrasonic array data using the total focusing method. Insight, Non-Destr Test Cond Monit 2004;46(11):677–80. http://dx.doi.org/10.1784/insi.46.11.677.52285.

[13] Kerr W, Rowe P, Pierce SG. Accurate 3D reconstruction of bony surfaces using ultrasonic synthetic aperture techniques for robotic knee arthroplasty. Comput Med Imaging Graph 2017;58:23–32. http://dx.doi.org/10.1016/j.compmedimag.2017.03.002.

[14] Malkin RE, Franklin AC, Bevan RLT, Kikura H, Drinkwater BW. Surface reconstruction accuracy using ultrasonic arrays: Application to non-destructive testing. NDT E Int 2018;96(February):26–34. http://dx.doi.org/10.1016/j.ndteint.2018.03.004.

[15] McKee JG, Bevan RLT, Wilcox PD, Malkin RE. Volumetric imaging through a doubly-curved surface using a 2D phased array. NDT E Int 2020;113(August 2019):102260. http://dx.doi.org/10.1016/j.ndteint.2020.102260.

[16] Cosarinsky G, Cruza JF, Muñoz M, Camacho J. Optimized auto-focusing method for 3D ultrasound imaging in NDT. NDT E Int 2023;134(November 2022). http://dx.doi.org/10.1016/j.ndteint.2022.102779.

[17] Tarantola A. Inverse problem theory and methods for model parameter estimation. Society for Industrial and Applied Mathematics; 2005, http://dx.doi.org/10.1137/1.9780898717921, arXiv:https://epubs.siam.org/doi/pdf/10.1137/1.9780898717921 URL https://epubs.siam.org/doi/abs/10.1137/1.9780898717921.

[18] Kirkebø JE, Austeng A. Improved beamforming using curved sparse 2D arrays in ultrasound. Ultrasonics 2007;46(2):119–28. http://dx.doi.org/10.1016/j.ultras.2007.01.001, URL https://www.sciencedirect.com/science/article/pii/S0041624X07000029.

[19] Parrilla M, Anaya JJ, Fritsch C. Digital signal processing techniques for high accuracy ultrasonic range measurements. IEEE Trans Instrum Meas 1991;40(4):759–63. http://dx.doi.org/10.1109/19.85348.

[20] Pan S, Qin Z, Lan H, Badal J. Automatic first-arrival picking method based on an image connectivity algorithm and multiple time windows. Comput Geosci 2019;123(May 2018):95–102. http://dx.doi.org/10.1016/j.cageo.2018.12.001.

[21] Marsh D. Applied geometry for computer graphics and CAD. Springer undergraduate mathematics series, Springer London; 2006, URL https://books.google.es/books?id=5wHxT5W424QC.

[22] Baker M. Alhazen's problem. Amer J Math 1881;4(1):327–31, URL http://www.jstor.org/stable/2369168.

[23] Fujimura M, Mocanu M, Vuorinen M. The ptolemy–alhazen problem and quadric surface mirror reflection. Complex Var Elliptic Equ 2022;1–19. http://dx.doi.org/10.1080/17476933.2022.2084537.

[24] Hecht E. Optics. Pearson; 2012, URL https://books.google.es/books?id=wcMWpBMMzIkC.